Relativistic extended Thomas-Fermi calculations of finite nuclei with realistic nucleon-nucleon interactions

M. Centelles, X. Viñas, and M. Barranco
Departament d'Estructura i Constituents de la Matèria, Facultat de Física, Universitat de Barcelona, Diagonal 647, E-08028 Barcelona, Spain

N. Ohtsuka,* Amand Faessler, Dao T. Khoa, and H. Müther
Institut für Theoretische Physik, Universität Tübingen, Auf der Morgenstelle 14, D-7400 Tübingen, Germany
(Received 6 October 1992)

A relativistic energy density functional is constructed to investigate the Dirac effects on different properties of the structure and scattering of finite nuclei. The kinetic energy density has been derived within a relativistic extended Thomas-Fermi model and includes gradient corrections to second order in $\hbar$. The effective mass and the volume term of the potential energy density have been obtained from a local density approximation to Dirac-Brueckner calculations of nuclear matter carried out with a realistic nucleon-nucleon interaction. This volume term is supplemented by the Coulomb energy and by conventional phenomenological surface and symmetry terms, and the few free parameters of the functional are suitably adjusted. Attention is then focussed on the calculation of fission barriers of rotating nuclei and of the complex optical potential for heavy ion collisions at intermediate energies. It turns out that the effects of the density-dependent Dirac spinor which have been incorporated in this approach allow for a reasonable description of the investigated properties.

PACS number(s): 24.10.Jv, 25.70.Bc, 24.75.+i

I. INTRODUCTION

In recent years the understanding of nuclear matter properties starting from a realistic nucleon-nucleon (NN) interaction fitted to NN scattering data has considerably been improved by the recognition of the importance of relativistic effects in treating nucleons inside a nucleus. The key point has been the observation that the dominant attractive and repulsive components of a realistic NN interaction exhibit different properties under a Lorentz transformation. Within the one-boson-exchange (OBE) model, the strong attractive component of the NN interaction is described in terms of a scalar σ-meson exchange, while the repulsive component is dominantly due to the exchange of the ω meson, a vector meson. This structure of the NN interaction implies that the self-energy of the nucleons in nuclear matter, calculated from this interaction, contains a strong attractive scalar component and a strong repulsive component which, in the rest frame of nuclear matter, transforms in the same way as the timelike component of a Lorentz vector. Inserting this self-energy into the Dirac equation for the nucleons inside the nuclear medium, one obtains solutions for which the small component of the Dirac spinor is drastically enhanced as compared to the Dirac spinors for the free nucleons. This enhancement of the small component of the Dirac spinor for a nucleon at finite densities can be described in terms of an effective nucleon mass m^* which is smaller than its bare mass. As a consequence of this change of the Dirac spinors for the nucleons as a function of the nuclear density, the matrix elements for the NN interaction and the kinetic energy are modified in the nuclear medium. These modifications are very important to describe the saturation properties of nuclear matter within a microscopic many-body calculation starting from a realistic NN interaction [1–6].

The works of Miller and Green [7] and of Brockmann [8] showed that the Dirac phenomenology could provide an acceptable description of spherical nuclei starting from relativistic OBE potentials. Microscopic Dirac-Brueckner-Hartree-Fock (DBHF) calculations have been carried out for the finite nucleus ^{16}O [9] using the Bonn potential [2,3,6] as the bare NN interaction. Also in this case the relativistic features just mentioned lead to better results than the corresponding Brueckner-Hartree-Fock (BHF) ones [10]. For finite nuclei, however, the relativistic effects considered in the DBHF approach are not sufficient to yield complete agreement of the calculated binding energy *and* radii with the experimental data. Besides these attempts to solve the DBHF equations directly for finite nuclei, there exist also calculations of ground-state properties of finite nuclei assuming a local density approximation (LDA) for the Dirac-Brueckner self-energies [11].

A more phenomenological approach has reached considerable success in the relativistic description of nuclear matter and the structure of finite nuclei as well. This approach starts from an effective meson-nucleon Lagrangian whose coupling constants and some meson

*Permanent address: Onomichi Junior College, Hisayamadacho 1600, Onomichi 722, Japan.

 ©1993 The American Physical Society

masses are adjusted to the properties of nuclear matter and finite nuclei (see Refs. [12] and [13] for a comprehensive survey). Solutions of these models in the relativistic Hartree (see, e.g., [14–17]) and Hartree-Fock (HF) [18, 19] approximations are available for finite nuclei. These models constitute the relativistic analog of the nonrelativistic HF method with density-dependent interactions such as the Skyrme [20, 21] and Gogny [22] forces. It may be stated [16, 17] that relativistic mean field (RMF) models of reasonable sophistication achieve about the same agreement with experiment compared with the more elaborated density-dependent forces in the nonrelativistic HF approximation, with the conceptual advantage of being fully relativistic and thus automatically incorporating the spin-orbit force, which is of fundamental importance in nuclear physics. Calculations with effective Lagrangians whose parameters are fitted to Dirac-Brueckner self-energies obtained in nuclear matter have also been performed [23–26].

Heavy ion (HI) scattering and large nuclear deformations are typical examples of the low and intermediate energy nuclear aspects which have been less explored using RMF methods. Axially deformed nuclei have been studied in Refs. [17,27–31] and dynamical calculations of nuclear collisions were investigated in [32, 33] using a Hartree RMF model. The only calculations of HI optical potentials on the basis of the microscopic Dirac-Brueckner formalism have been carried out by the Tübingen group [34].

In this work we intend to employ the Dirac-Brueckner results on nuclear matter of Ohtsuka *et al.* [34] to evaluate the fission barriers of some selected nuclei and the complex optical potential for some HI systems at intermediate incident energies. For this purpose we shall use a LDA to build an energy density functional. The potential part comes from a microscopic calculation using a modern version of the realistic Bonn NN interaction, which incorporates the effects of Brueckner correlations and Dirac effects. The kinetic part is taken from a relativistic extended Thomas-Fermi (RETF) approximation that incorporates gradient corrections of order $\hbar^2$ [35, 36]. The Coulomb energy and two standard correction terms which account in part for the surface and neutron-proton asymmetry effects are added to the volume term of the potential energy density of the functional. With respect to Ref. [34], the main improvement is that the use of the present energy density functional will allow us to obtain fully self-consistent nuclear densities by solving the corresponding Euler-Lagrange equations, instead of using parametrized densities as in this reference. With respect to the previous work on fission barriers by Garcias *et al.* [37], the use here of a RMF method represents a sizable improvement, since in this reference a nonrelativistic NN interaction was used that did not reproduce the nuclear matter saturation point, which is typical for all nonrelativistic G-matrix calculations [5, 10].

This paper is organized as follows. In Sec. II we summarize the way the DBHF potential energy density has been obtained, construct the complete energy density functional, and adjust its few free parameters, showing the results for finite nuclei. In Sec. III we calculate the fission barriers for some selected nuclei, with emphasis on the angular momentum dependence of these barriers. The HI potentials are obtained in Sec. IV, and some illustrative elastic HI scattering cross sections are calculated. Finally, we draw the conclusions in Sec. V. A preliminary account of this work has been presented elsewhere [38].

II. RELATIVISTIC ENERGY DENSITY FUNCTIONAL

A. DBHF potential energy density

The nucleon Dirac spinor $\tilde{u}(\mathbf{k},\rho)$ for a nucleon of momentum $\mathbf{k}$ in nuclear matter of density ρ is determined by solving a Dirac equation

$$[\gamma^\mu k_\mu - m - \Sigma(\mathbf{k},\rho)]\,\tilde{u}(\mathbf{k},\rho) = 0\,, \tag{2.1}$$

where m is the free nucleon mass, γ^μ are the Dirac matrices, and $\Sigma(\mathbf{k},\rho)$ is the self-energy operator of the nucleon. For symmetric nuclear matter this self-energy contains a large scalar component and a term, which, in the rest frame of nuclear matter, transforms in the same way as the timelike component of a Lorentz vector:

$$\Sigma(\mathbf{k},\rho) = A(\mathbf{k},\rho) + \gamma_0\, B(\mathbf{k},\rho)\,. \tag{2.2}$$

In a simple RMF or Hartree approximation to the field theoretical model for the meson-nucleon many-body system, the coefficients $A(\mathbf{k},\rho)$ and $B(\mathbf{k},\rho)$ are independent of the momentum $\mathbf{k}$ and are directly related to the attractive scalar and repulsive vector meson exchange contributions, respectively. Using a self-energy of the form given in Eq. (2.2), the solution of Eq. (2.1) for a positive energy nucleon is explicitly given by

$$\tilde{u}(\mathbf{k},\rho) = \left(\frac{\varepsilon + m^*}{2\varepsilon}\right)^{1/2} \begin{pmatrix} 1 \\ \dfrac{\boldsymbol{\sigma}\cdot\mathbf{k}}{\varepsilon + m^*} \end{pmatrix} \chi_\sigma\,, \tag{2.3}$$

where $m^* = m + A(\mathbf{k},\rho)$ is the nucleon effective mass and $\varepsilon = (k^2 + m^{*2})^{1/2}$. χ_σ is a Pauli spinor and the normalization is

$$\tilde{u}^\dagger(\mathbf{k},\rho)\,\tilde{u}(\mathbf{k},\rho) = 1\,. \tag{2.4}$$

In the Dirac-Brueckner approach, $\Sigma(\mathbf{k},\rho)$ is defined in terms of the G matrix $\tilde{G}$ as

$$\langle \mathbf{k}|\Sigma|\mathbf{k}\rangle = \sum_{\text{spin, isospin}} \int_F \frac{d\,\mathbf{k}'}{(2\pi)^3} \langle \mathbf{k}\mathbf{k}'|\tilde{G}(W = \epsilon_k + \epsilon_{k'})|\mathbf{k}\mathbf{k}'\rangle\,. \tag{2.5}$$

The integration is carried out over the Fermi sphere for nuclear matter of the density under consideration. The G matrix $\tilde{G}$ is the solution of the relativistic Bethe-Goldstone equation for nuclear matter *at rest.* It is worth mentioning that, in addition to the self-consistent treatment of the starting energy W which is required in the nonrelativistic BHF approach, the DBHF approach furthermore needs to treat the Dirac spinors self-consistently [2]. The spinors (2.3) resulting from Eq. (2.1) have to be used in evaluating the matrix elements

of the NN potential in the nuclear medium. We have taken as the bare NN interaction the Bonn potential of Refs. [2, 3], which was already used by Ohtsuka *et al.* in [34]. Employing Eq. (2.2) for $\Sigma(\mathbf{k},\rho)$, one finds that $A(\mathbf{k},\rho)$ and $B(\mathbf{k},\rho)$ are independent of the momentum $\mathbf{k}$ to a very good approximation [24]. The $\mathbf{k}$-independent functions $A(\rho)$ and $B(\rho)$ are obtained by a fit to the numerical values for the self-energy of Eq. (2.5) as follows [2]:

$$\langle \mathbf{k}|\Sigma|\mathbf{k}\rangle \approx A(\rho) + B(\rho) - \left(1 - \frac{m}{m^*}\right)\frac{k^2}{2m^*} . \tag{2.6}$$

Consequently, the spinors of Eq. (2.3) can be parametrized in terms of a nucleon effective mass m^* which depends on ρ but not on $\mathbf{k}$.

The potential energy density is readily obtained from the self-energy as

$$\Pi(\rho) = \frac{4}{2}\int_F \frac{d\mathbf{k}}{(2\pi)^3}\langle \mathbf{k}|\Sigma(\mathbf{k},\rho)|\mathbf{k}\rangle . \tag{2.7}$$

In the relativistic treatment of nuclear matter, the kinetic energy density is given by

$$\begin{aligned}\tau(\rho) &= 4\int_F \frac{d\mathbf{k}}{(2\pi)^3}\tilde{u}^\dagger(\mathbf{k},\rho)\ (\boldsymbol{\alpha}\cdot\mathbf{k} + \beta m - m)\,\tilde{u}(\mathbf{k},\rho) \\ &= 4\int_F \frac{d\mathbf{k}}{(2\pi)^3}\left(\frac{k^2 + mm^*}{\varepsilon} - m\right) . \end{aligned} \tag{2.8}$$

The relativistic approach makes the kinetic energy of nuclear matter less repulsive than in the nonrelativistic approach, while on the other hand the potential energy (2.7) becomes much less attractive. As a sum, the total energy becomes less attractive at high density and the empirical values of binding energy and density of the nuclear matter saturation point can be reproduced.

B. RETF kinetic energy density

For any application to finite nuclei it is desirable to have a kinetic energy density which incorporates some features not present in the simple functional (2.8). A kinetic energy density that includes up to $\hbar^2$-order corrective terms has recently been derived in a RETF semiclassical approximation to the nuclear problem described by a scalar-vector Dirac Hamiltonian [35, 36]. Previously, the result was known for the atomic case in which $m^* = m$ [39]. In the relativistic semiclassical context, Weigel, Haddad, and Weber [40] have worked out expressions for the Wigner-Kirkwood expansion of the HF approximation to a Lagrangian of OBE potential structure, and Speicher, Dreizler, and Engel [41] have studied the density functional approach to quantum hadrodynamics.

For each kind of nucleons q (neutrons or protons), the RETF kinetic energy density [35, 36] is written as

$$\tau_q(\rho_q, m^*) = \tau_{0,q}(\rho_q, m^*) + \tau_{2,q}(\rho_q, m^*, \boldsymbol{\nabla}\rho_q, \boldsymbol{\nabla}m^*) . \tag{2.9}$$

The explicit expressions of the term $\tau_{0,q}$, which in the nuclear matter limit would correspond to (2.8), and of the contribution $\tau_{2,q}$ are given in the Appendix. Note that in our approach the nucleon effective mass m^* depends only on the total density $\rho = \rho_n + \rho_p$.

The corrective term $\tau_{2,q}$ has several interesting features. First of all, its inclusion in τ_q allows one to obtain *fully variational* nucleon densities that go to zero exponentially, contrary to what happens if only the $\hbar^0$-order term $\tau_{0,q}$ is kept [12]. Second, nonlocal spin-orbit and effective mass corrections are automatically taken into account in τ_q up to order $\hbar^2$. This is conceptually important in a relativistic formalism, and may be of some practical importance because of the large variations for m^*/m in the relativistic case, as this ratio goes from ≤ 0.6 at saturation to ~ 1.0 at low densities. A detailed account of the RETF method applied to σ-ω models, as well as a comparison with the corresponding Hartree results, can be found in [36, 42].

C. Complete energy density functional and parameter fit

The total energy of a nucleus in terms of the energy density functional $\mathcal{E}$ is given by

$$E = \int d\mathbf{r}\,\mathcal{E}\left[\rho_q(\mathbf{r}), \tau_q(\mathbf{r})\right] , \tag{2.10}$$

where

$$\begin{aligned}\mathcal{E}(\rho_q,\tau_q) = &\sum_q \tau_q + \alpha\Pi(\rho) \\ &+ C_{\rm sym}(\rho_n - \rho_p)^2 + \eta(\boldsymbol{\nabla}\rho)^2 + \mathcal{E}_{\rm Coul}(\rho_p) .\end{aligned} \tag{2.11}$$

The terms τ_q and $\Pi(\rho)$ have been defined in the previous subsections. The last three terms in (2.11) are purely phenomenological. The first one is a potential symmetry energy term, the gradient term accounts for a part of the surface energy, and the Coulomb energy $\mathcal{E}_{\rm Coul}(\rho_p)$ contains a direct term and a exchange term in the standard Slater approximation. As discussed below, the constant α in front of the potential energy density $\Pi(\rho)$ will be used to improve on the finite nuclei results. Altogether, the functional contains three free parameters α, $C_{\rm sym}$, and η. Despite the phenomenological character that these parameters give to the energy density (2.11), a connection with the microscopic calculation is kept in the model inasmuch as it is the density-dependent Dirac spinor, microscopically derived in the DBHF approach, which determines the behavior of Π and τ_q (through m^*) as a function of the density.

The nuclear symmetry energy has been obtained by performing DBHF calculations of symmetric nuclear matter and neutron matter [43] (see also [44]). In principle, this could be used to fix the $C_{\rm sym}$ parameter, and putting $\alpha = 1$ we would have been left with only one free parameter η. However, the NN interaction used in [43] is different from the one used by Ohtsuka *et al.* [34], for which m^* and $\Pi(\rho)$ are available for many values of the density and also for two systems of nuclear matter

in relative motion. Since we want to perform a calculation of the optical potential for two colliding nuclei using the functional (2.11), we have taken $\Pi(\rho)$ from the latter reference and have left $C_{\rm sym}$ as a free parameter. The functional (2.11), made up of the $\hbar^2$-order kinetic part and a potential part which contains the minimal phenomenology to make the whole functional realistic, has to be considered as a single package, which constitutes our RETF model.

The Euler-Lagrange variational equations corresponding to the functional $\mathcal{E}(\rho_q, \tau_q)$ are solved self-consistently using the imaginary time-step method as described in Refs. [36, 45], once a value for the set of parameters $(\alpha, C_{\rm sym}, \eta)$ has been chosen. We shall present the results obtained with three different functionals. The first one will be called TU0 and corresponds to the parameter-free case $\eta = C_{\rm sym} = 0$ and $\alpha = 1$. This functional, which is the closest one to a microscopic calculation, in general, is not expected to yield good results when compared to experiment because it lacks some surface and symmetry energy. It is interesting, however, to know how far one can go without including any kind of phenomenology in the model. TU1 is the second functional; to fix its parameters we have adjusted the binding energy of ^{40}Ca and ^{208}Pb, and the *semiclassical* fission barrier (B_f) of ^{240}Pu, which is $\sim$ 3.8 MeV [46, 47] (details about the fission barrier calculation are given in Sec. III). For actinide nuclei shell effects play an important role and may originate a double-humped structure in the fission barrier as in the case of ^{240}Pu. Of course, the fission barriers calculated with our approach have no shell structure and can show only one smooth maximum. Therefore, we have to compare our calculation with the value of the fission barrier which is obtained after shell effects have been subtracted by shell-correction methods [46]. The parameters of the third functional, called TU2, have been adjusted to reproduce the binding energy of ^{40}Ca and ^{208}Pb, and the value of the surface energy of semi-infinite symmetric nuclear matter corresponding to the Skyrme SkM* force, $E_s = 17.22$ MeV [47] (let us recall that this makes SkM* able to reproduce the semiclassical fission barrier of ^{240}Pu).

Table I collects the values of the parameters and the nuclear matter characteristics of the three functionals, as well as the calculated fission barrier of ^{240}Pu. It is very simple to obtain the surface tension σ of semi-infinite symmetric nuclear matter for functionals such as that of Eq. (2.11). Neglecting the Coulomb energy and taking $\rho_n = \rho_p = \rho/2$, Eq. (2.11) can be written as

$$\mathcal{E}(\rho) = C(\rho) + [D(\rho) + \eta](\nabla\rho)^2 , \tag{2.12}$$

where

$$C(\rho) = \sum_q \tau_{0,q}(\rho_q = \rho/2) + \alpha\Pi(\rho) , \tag{2.13}$$

and $D(\rho)$ is defined such that

$$D(\rho)(\nabla\rho)^2 \equiv \sum_q \tau_{2,q}(\rho_q = \rho/2) . \tag{2.14}$$

For a system with a planar surface perpendicular to the z axis, $\rho = \rho(z)$, and using the method outlined in Ref. [48] one gets

$$\sigma = \int_{-\infty}^{+\infty} dz \left[\mathcal{E}(\rho) - \frac{E}{A}\rho\right]$$

$$= 2\int_0^{\rho_0} d\rho \left[C(\rho) - \frac{E}{A}\rho\right]^{1/2} [D(\rho) + \eta]^{1/2} , \tag{2.15}$$

where E/A is the energy per particle at the saturation density ρ_0. The surface energy is

$$E_s = 4\pi r_0^2 \sigma , \tag{2.16}$$

where $r_0 = [3/(4\pi\rho_0)]^{1/3}$ is the nuclear matter radius.

The (bulk) symmetry energy is obtained by expanding the energy per particle of asymmetric nuclear matter for small values of the relative neutron excess $(\rho_n - \rho_p)/\rho$. The result for the functional (2.11) is

$$E_{\rm sym} = \frac{k_F^2}{6\varepsilon_F}\left[1 - \frac{mm^*}{\varepsilon_F^2}\left(1 - \frac{m^*}{m}\right)\right] + C_{\rm sym}\,\rho , \tag{2.17}$$

TABLE I. Parameters $(\alpha, C_{\rm sym}, \eta)$ of the TU0, TU1, and TU2 functionals, their nuclear matter properties (energy per particle E/A, particle density ρ_0, Fermi momentum k_F, incompressibility κ, effective mass m^*/m, and volume symmetry energy $E_{\rm sym}$ at saturation), surface energy E_s of semi-infinite symmetric nuclear matter, and fission barrier B_f of ^{240}Pu.

	TU0	TU1	TU2
α	1.0	1.024	1.036
$C_{\rm sym}$ (MeV fm^3)	0.0	84.0	118.0
η (MeV fm^5)	0.0	8.20	15.25
E/A (MeV)	−15.17	−15.90	−16.27
ρ_0 (fm^{-3})	0.1780	0.1778	0.1777
k_F (fm^{-1})	1.381	1.381	1.380
κ (MeV)	239.2	250.2	255.7
m^*/m	0.616	0.616	0.616
$E_{\rm sym}$ (MeV)	9.48	24.41	30.45
E_s (MeV)	13.97	15.83	17.22
B_f (MeV)	2.2	3.7	5.6

evaluated at $\rho = \rho_0$. k_F is the Fermi momentum and $\varepsilon_F = (k_F^2 + m^{*2})^{1/2}$. The first term on the right hand side of Eq. (2.17) comes from $\tau(\rho)$, and the second term from the phenomenological potential symmetry energy.

Table I shows that the nuclear matter properties of the three functionals are well within the commonly accepted values, except for a rather small symmetry energy $E_{\rm sym}$ in the TU0 case and, less markedly, in the TU1 case. The symmetry energy of TU0 is so small because for this functional only the kinetic energy contributes to it (the potential energy is calculated for $\rho_p = \rho_n$). The binding energies and charge radii we have obtained for some nuclei with the functionals TU0, TU1, and TU2 are displayed in Table II. The calculated total energies have been corrected for spurious effects of center-of-mass motion by subtracting the kinetic energy per particle, as is usually done in non-relativistic calculations. The charge radii have been obtained from the proton radii as $r_c = (r_p^2 + 0.8^2)^{1/2}$ fm using a form factor for the proton charge. One may see from this table that the agreement between our calculations and the experimental data is globally good, especially for the binding energies. Even the parameter-free functional TU0 yields acceptable results. However, the binding energy estimate for the nucleus ^{40}Ca obtained with TU0 is too small compared with the experimental value, and is necessary to set $\alpha > 1$ if one wants to fit it, as in TU1 and TU2. It is worthwhile noting the very small change ($\alpha \approx 1$, Table I) we have introduced in the potential part of both the TU1 and TU2 functionals. We want to point out again that as the spin orbit is a fully relativistic effect, our expression for the kinetic energy density functional τ_q automatically incorporates the $\hbar^2$-order corrections of spin-orbit origin to this energy.

The TU0 functional gives good binding energies for the smaller systems ^{12}C and ^{16}O, without it being necessary to add surface energy or, obviously, symmetry energy. We point out that, compared with relativistic Hartree results, relativistic semiclassical calculations of order $\hbar^2$ yield some overbinding [36, 42]. This is the reason why the binding energy of ^{16}O obtained with TU0 in this RETF approximation is in better agreement with the experimental value than the fully microscopic DBHF result [9]. With increasing neutron excess, the agreement of TU0 with experiment is spoiled. As TU0 has a small surface tension, it underestimates the semiclassical fission barrier of ^{240}Pu (cf. Table I) and that of any other nucleus, consequently. The TU2 force, which has the higher surface energy, yields slightly better results than TU0 and TU1, at the price of overestimating the semiclassical fission barrier of ^{240}Pu.

The TU0 parametrization gives better charge radii than TU1 and TU2. This may be understood in the following terms. The lack of symmetry energy of TU0 is unable to counterbalance the Coulomb repulsion among protons. As a consequence, the proton density spreads out at the price of yielding unrealistically compact neutron densities. For example, the neutron rms radius of ^{208}Pb is 5.29 fm for TU0 and 5.44 fm for TU1 (a HF calculation with the SkM* force gives 5.63 fm [45]). In any case, the calculated charge radii are systematically smaller than the experimental ones. This might be due to the fact that also the saturation density of nuclear matter calculated in the DBHF approximation is slightly above the empirical value (see Table I). Note, however, that the radii we have found with the present RETF method are in much better agreement with the experimental ones than when one uses a nonrelativistic G-matrix calculation as the input to obtain $\Pi(\rho)$ [37].

III. FISSION BARRIERS

In this section we shall apply the TU1 functional to the semiclassical description of symmetric nuclear fission. We shall not present here results obtained with TU0 and TU2 because these functionals are unable to give a correct quantitative description of fission barriers, as discussed above in the case of ^{240}Pu (Table I). Compared with TU1, TU0 yields too small barriers whereas with TU2 they are too high. This effect, which is especially appreciable for heavy nuclei, is a direct consequence of the value of the η parameter (i.e., of the surface tension) of the functional, since fission takes place through a delicate balance between the opposing actions of the Coulomb repulsion and the surface tension as the nucleus is deforming.

The basic ingredients of the method we use have been described in [37] and references quoted therein. It

TABLE II. Binding energies B (in MeV) and charge radii r_c (in fm) obtained with the TU0, TU1, and TU2 functionals in comparison with experimental data.

	TU0		TU1		TU2		Exp	
	B	r_c	B	r_c	B	r_c	B	r_c
^{12}C	94.2	2.49	94.3	2.53	92.4	2.57	92.2	2.47
^{16}O	128.3	2.66	129.4	2.69	127.5	2.73	127.6	2.73
^{40}Ca	333.1	3.36	342.3	3.37	342.2	3.40	342.1	3.49
^{48}Ca	420.5	3.48	422.5	3.46	419.9	3.47	416.0	3.48
^{56}Ni	461.1	3.70	476.9	3.70	479.0	3.72	484.0	3.75
^{90}Zr	759.4	4.22	779.7	4.18	783.8	4.19	783.9	4.27
^{114}Sn	942.1	4.53	967.2	4.49	973.7	4.50	971.6	4.61
^{118}Sn	988.3	4.57	1006.0	4.52	1010.0	4.53	1005.0	4.64
^{140}Ce	1157.5	4.81	1172.1	4.76	1176.0	4.77	1172.7	4.88
^{208}Pb	1641.6	5.46	1636.6	5.39	1636.5	5.39	1636.5	5.50

is based on a two-dimensional (2D), axially symmetric Thomas-Fermi model that incorporates rotational effects. To describe the symmetric fission of a nucleus, we have parametrized the fission path by a single collective coordinate, namely, the quadrupole moment Q. To obtain the equilibrium density at given values $Q = Q_0$ of the deformation and L_x of the angular momentum, we have minimized the total energy with the usual constraints on Q and L_x:

$$E + \tfrac{1}{2}\lambda\left(\langle Q\rangle - Q_0\right)^2 - \omega\langle L_x\rangle\,, \tag{3.1}$$

where E is given by Eqs. (2.10) and (2.11), and the Lagrange multiplier ω is to be identified with the angular velocity about the rotation axis x. We have imposed axial symmetry about the z axis, and have solved the Euler-Lagrange equations corresponding to (3.1) in cylindrical coordinates (r, z) employing the imaginary time-step method. It has been checked that the agreement that is obtained between 1D and 2D calculations of spherical nuclei is better than 1–2 MeV in the total energy for the nuclei we have studied.

Rotation has been considered in the rigid-body approximation [49]. At a given deformation, the moment of inertia I_x, needed to compute the rigid angular velocity

$$\omega = \frac{\langle L_x\rangle}{I_x} \tag{3.2}$$

and the rotational energy

$$E_{\rm rot} = \frac{\langle L_x\rangle^2}{2I_x}\,, \tag{3.3}$$

is obtained from the self-consistent variational density $\rho(r, z)$:

$$I_x = m\iint 2\pi r dr dz\left[z^2 + \frac{r^2}{2}\right]\rho(r, z)\,. \tag{3.4}$$

Similarly, the quadrupole moment is computed as

$$\langle Q\rangle = \iint 2\pi r dr dz\left[2z^2 - r^2\right]\rho(r, z)\,. \tag{3.5}$$

We collect in Table III the saddle-point characteristics (barrier height B_f and quadrupole moment Q_s) and the L_c values that have been obtained with the parametrization TU1 for six nuclei, ranging from the light ^{52}Fe to the heavy ^{240}Pu. The RETF results are compared with the ones we have obtained using the SkM* force in a nonrelativistic Thomas-Fermi calculation of order $\hbar^2$. The corresponding liquid droplet values [50, 51] are also shown. It can be seen that all three methods yield comparable results. The quadrupole moment of the saddle point is an increasing function of the nuclear mass, except for the heaviest systems, and the highest fission barriers correspond to nuclei with $A \sim 100$ [49].

Figure 1 is a three-dimensional plot of the closest-to-saddle configurations that we have calculated with TU1 for the six considered nuclei, without rotation. Some equidensity lines in the (x, z) plane, corresponding to these configurations, are shown in Fig. 2. These figures show the known fact that the saddle configuration of a

TABLE III. Fission barrier B_f (in MeV), quadrupole moment of the saddle point Q_s (in barns), and critical angular momentum L_c (in units of $\hbar$), obtained with the TU1 functional in the RETF approach, with the SkM* force [47] in a $\hbar^2$-order nonrelativistic Thomas-Fermi calculation, and with the liquid droplet model [50, 51].

		TU1	SkM*	LD
^{52}Fe	B_f	47.7	49.0	48.0
	Q_s	28	29	
	L_c	48	55	50
^{118}Sn	B_f	56.5	55.6	52.6
	Q_s	119	140	
	L_c	102	101	95
^{152}Dy	B_f	36.4	34.1	36.7
	Q_s	180	200	
	L_c	87	91	95
^{186}Os	B_f	25.2	20.8	22.5
	Q_s	235	270	
	L_c	81	75	90
^{207}Bi	B_f	13.8	9.2	12.2
	Q_s	183	210	
	L_c	74	73	85
^{240}Pu	B_f	3.7	3.9	3.0
	Q_s	91	120	
	L_c	58	50	75

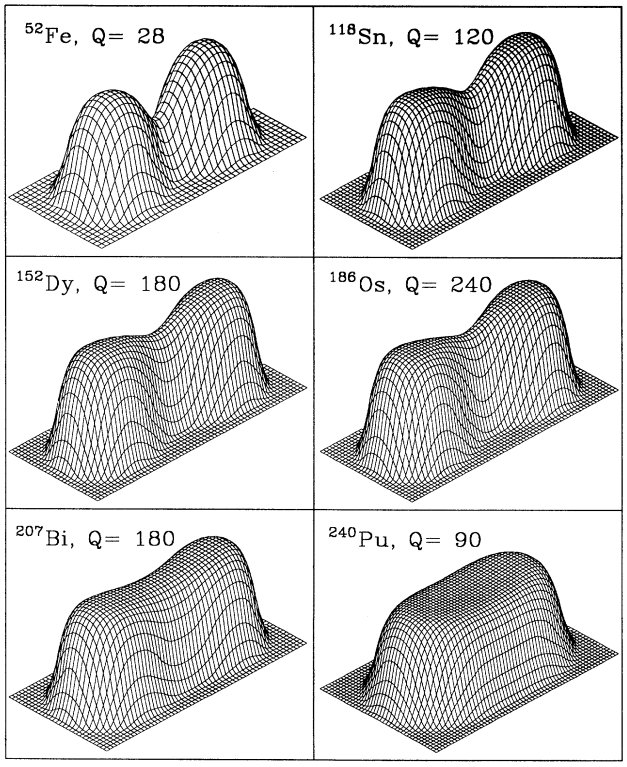

FIG. 1. Three-dimensional isometric view of the density ρ, plotted versus the (x, z) plane, for the closest-to-saddle configurations that we have calculated without rotation using the TU1 functional. The corresponding quadrupole moment Q (in barns) is indicated for each nucleus.

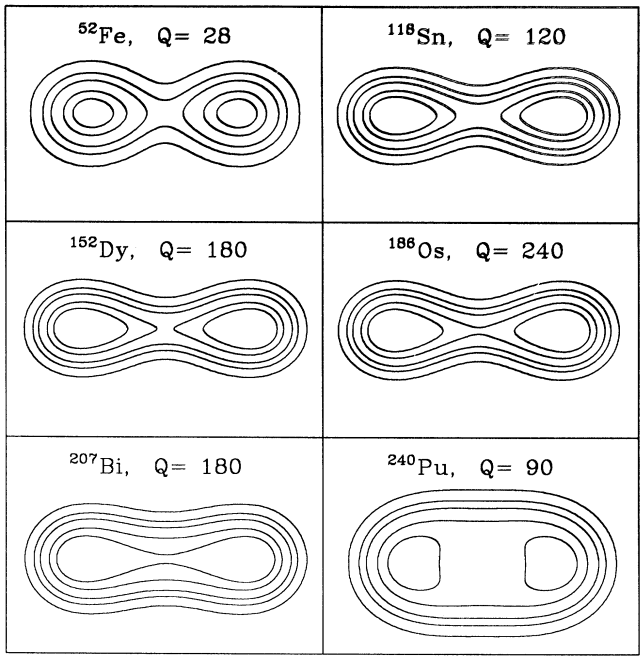

FIG. 2. Equidensity lines in the (x, z) plane corresponding to the configurations plotted in Fig. 1. From outside to inside, the lines represent contours of constant density $\rho = 0.01$, 0.06, 0.11, 0.15, and 0.165 fm^{-3}.

heavy nucleus is rather compact, whereas it is quite elongated for a light nucleus. The equidensity lines are parallel to a good approximation except those corresponding to high densities in the neck region. Similar contour plots of the saddle-point shape for some nuclei can be found in [52], where a Thomas–Fermi model is applied to the calculation of fission barriers.

The evolution of the fission barrier as a function of the angular momentum is displayed in Fig. 3 for the nucleus

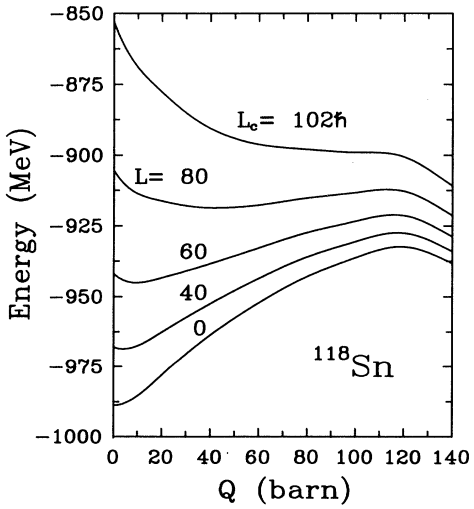

FIG. 3. Angular momentum dependence of the fission barrier of ^{118}Sn as a function of the quadrupole moment Q (with TU1).

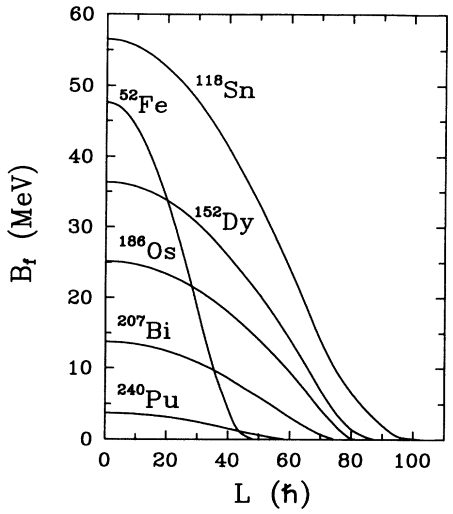

FIG. 4. Stability diagram showing the evolution of the fission barrier height as a function of the angular momentum L (with TU1).

^{118}Sn, which has a critical angular momentum $L_c = 102\hbar$ in our model. As rotation gets faster, it is seen that the configuration of minimum energy is no longer spherical and corresponds to a deformed shape. Finally, more detailed information about the L dependence of the fission barrier height is given in Fig. 4, which represents the stability diagram of the nuclei we have studied. Intermediate mass nuclei can bear higher L values before the fission barrier disappears [49] (see also Table III).

IV. HEAVY ION OPTICAL POTENTIALS AT INTERMEDIATE ENERGIES

Using nuclear matter theory and the energy density formalism, the real and imaginary parts of the optical potential between two nuclei have been derived from realistic NN interactions by the Tübingen group in nonrelativistic [53, 54] and relativistic [34] approaches. These complex optical potentials have been successfully applied to describe the HI scattering data at intermediate energies. Therefore, it is of interest to see if the present model, which has been shown to give a satisfactory description of finite nuclei and fission barriers, can be used to improve on the relativistic calculation of the HI optical potential.

The optical potential between two nuclei at separation distance R has been calculated as

$$U(K_r, R) = E(K_r, R) - E(K_r, \infty)\,, \tag{4.1}$$

using the sudden approximation for the density distribution of the composite system. In Eq. (4.1), $E(K_r, R)$ is the total energy of the system formed by two nuclei whose centers are at distance R, approaching each other at such relative energy that the centers of the two Fermi spheres which represent the local densities of the target and the projectile are at a distance K_r (the relative momentum).

To obtain the potential energy density, it is assumed

that the collision can be locally represented by a system of two nuclear matters colliding with relative momentum K_r, and the total energy of the composite system is calculated using the nuclear densities obtained in Sec. II following the method indicated in [34]. That is, instead of solving the relativistic Bethe-Goldstone equation for two colliding systems of nuclear matter, the following steps are taken. First, the relativistic Bethe-Goldstone equation is solved for a single nuclear matter of density ρ at rest, and the effective mass $m^*(\rho)$ and the matrix elements of the bare NN interaction between two nucleons in nuclear matter are determined in the same way as it has been done in Refs. [2, 3], and which has been already used to obtain the potential part $\Pi(\rho)$ employed in the previous sections. Then, these relativistic matrix elements are used to solve a nonrelativistic Bethe-Goldstone equation for two systems of nuclear matter with the total density of the combined system. By this procedure, proposed by Ohtsuka *et al.* in [34], the relativistic effects arising from the change of the Dirac spinors in the nuclear medium are included in this nonrelativistic G matrix since the matrix elements of the bare NN interaction are evaluated with the modified spinors, Eq. (2.3).

Special attention has to be paid to the kinetic energy density in the case of two Fermi spheres in relative motion, and to the way to fix K_r for a given HI colliding system and incident energy. These matters are discussed in detail in [34] and references therein.

One of the nicest features of the microscopic G-matrix approach to HI collisions is that in the case of two systems of nuclear matter in relative motion, the potential energy becomes complex since two nucleons can be scattered into unoccupied states with conservation of their total momentum and energy. Thus one gets both the real and imaginary parts of the optical potential from the same interaction, and basically only the contributions of the mutual excitation of target and projectile are left out. As this contribution can be accounted for by standard coupled-channel techniques, the calculation of HI scattering cross sections becomes parameter free.

We have studied the systems $^{12}C + {}^{12}C$ at 1016, 1449, and 2400 MeV, $^{16}O + {}^{12}C$ at 1503 MeV, and $^{16}O + {}^{28}Si$ at 1503 MeV in the laboratory frame. Figure 5 displays the real and imaginary parts of the optical potential for $^{12}C + {}^{12}C$ obtained with the TU1 functional. The optical potentials that TU0 and TU2 yield are very similar to those of TU1, also for the systems $^{16}O + {}^{12}C$ and $^{16}O + {}^{28}Si$, and thus are not shown. There are only slight differences near the origin, but HI scattering is not sensitive to this region of the optical potential.

A detailed comparison of the results of Refs. [34] and [54] reveals that the relativistic treatment affects the real part of the HI potentials obtained from two systems of nuclear matter flowing through each other in a similar way as what happens for a single system of nuclear matter at rest. The change of the Dirac spinors reduces the attraction of the potential energy which is again counterbalanced by the reduction of the kinetic energy. The most striking feature of the relativistic approach to HI optical potentials is that the imaginary part is considerably enhanced at high densities. The change of the Dirac spinors reduces the attractive contributions of the σ-meson exchange but does not influence the repulsive ω-meson exchange. Therefore, two nucleons at high densities feel a larger short-range repulsion, which leads to more scattering into unoccupied states, i.e., to a larger imaginary part. Note that this relativistic effect that comes from the potential energy is not compensated by any effect from the kinetic energy, as happens for the real part.

The calculated optical potentials have been used to analyze some elastic HI scattering data. The elastic scattering cross sections have been obtained employing the PTOLEMY code [55] in the optical model (OM) or coupled-channel (CC) analysis. As we have indicated above, the calculated HI potentials include the effect of two-particle–two-hole (2p-2h) inelastic excitations, but not the excitation of 1p-1h collective states which are absent in nuclear matter due to momentum conservation. They can be taken into account either as an additional effective potential [56], or explicitly within the CC formalism. We

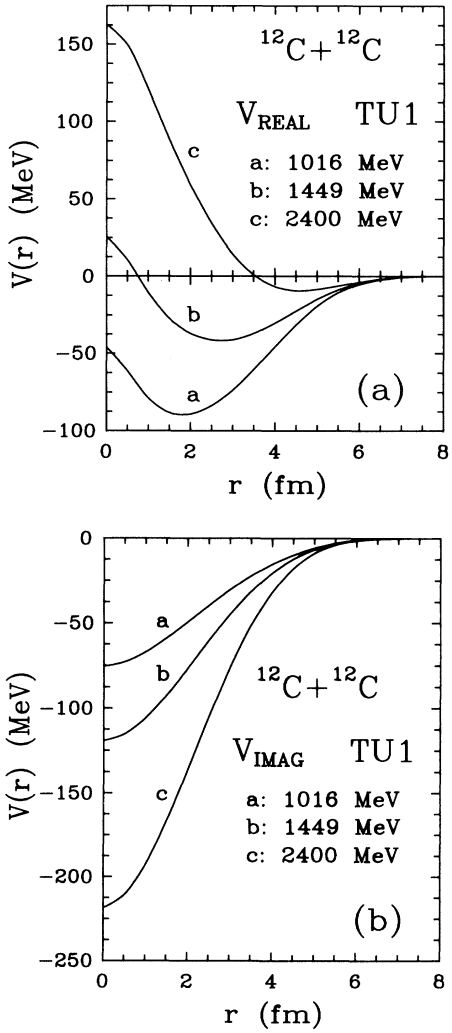

FIG. 5. (a) Real and (b) imaginary parts of the optical potential for $^{12}C + {}^{12}C$ at $E_{lab} = 1016$, 1449, and 2400 MeV, obtained with the TU1 functional.

have followed the latter approach, including the excitation of such collective states in both the target and the projectile.

The collective states we have included into the CC analysis in the case of $^{16}O + ^{28}Si$ are shown in the coupling scheme of Fig. 6. For the $^{12}C + ^{12}C$ system, we have included the first 2^+ (4.44 MeV) and 3^- (9.64 MeV) states in ^{12}C. The coupling interaction is obtained adopting the vibrational or rotational model for the nuclear excited states. To get the nuclear transition potential U_l for a given excited state, one needs to estimate the so-called nuclear deformation length $\beta_N R_N$. We have followed Blair's rule

$$\beta_N R_N = \beta_C R_C \tag{4.2}$$

to determine it. The deformation parameter β_C for the charge distribution is obtained from the electric transition probability $B(El)$ using

$$B(El) = \left[\frac{3}{4\pi} Z e R_C^l \beta_C(l)\right]^2 , \tag{4.3}$$

with $R_C = 1.2A^{1/3}$ fm. Then, the transition potential follows from

$$U_l(r) = \beta_N R_N \frac{dU_0(r)}{dr} , \tag{4.4}$$

where $U_0(r)$ is the complex optical potential previously determined. Thus, the CC calculations are essentially free of any adjustable parameter and constitute a good test of the reliability of the method.

Figures 7–11 show the elastic scattering cross sections for the systems $^{12}C + ^{12}C$ at $E_{lab} = 1016$, 1449, and 2400 MeV, $^{16}O + ^{12}C$ at $E_{lab} = 1503$ MeV, and $^{16}O + ^{28}Si$ at $E_{lab} = 1503$ MeV, respectively. The experimental data have been taken from Refs. [57–60]. For the systems $^{12}C + ^{12}C$ at $E_{lab} = 1016$ and 1449 MeV and $^{16}O + ^{28}Si$ at $E_{lab} = 1503$ MeV we display both the OM and the CC results, calculated with the TU1 functional. In the case of the systems $^{12}C + ^{12}C$ at $E_{lab} = 2400$ MeV and $^{16}O + ^{12}C$ at $E_{lab} = 1503$ MeV, we instead present only the CC analysis and compare the TU0, TU1, and TU2 results. The latter figures show that the three functionals yield comparable results for the cross sections of the systems under consideration. For this comparison one should be aware that the surface tension contents in TU1 and TU2 give an attractive contribution to the real part of the HI potential at the surface. This is counterbalanced by the global enhancement factor α in such a way that the real parts of the TU0, TU1, and TU2 potentials are very similar at the surface region which is most sensitive to HI scattering data. Consequently, the calculated TU0, TU1, and TU2 cross sections for elastic HI scattering are also very similar.

The figures show that our potentials reproduce the

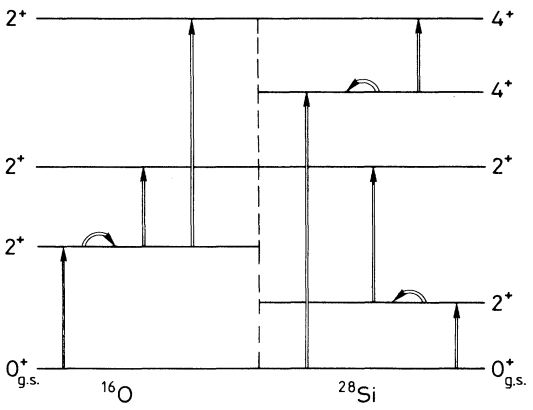

FIG. 6. Coupling scheme we have considered in the coupled channel calculation of the $^{16}O + ^{28}Si$ scattering.

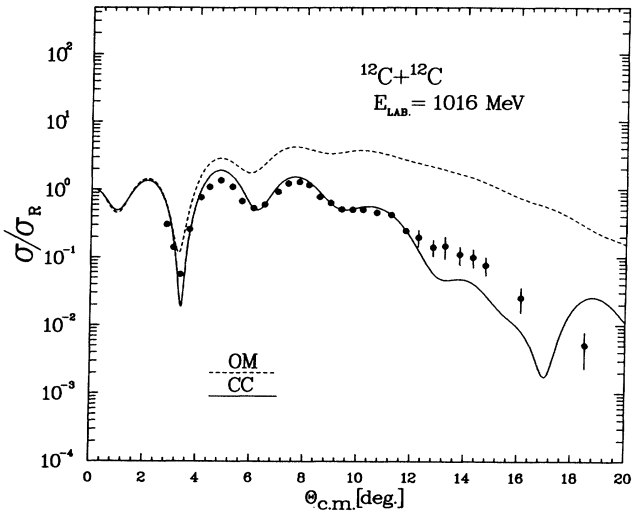

FIG. 7. Elastic scattering cross section for $^{12}C + ^{12}C$ at $E_{lab} = 1016$ MeV calculated with the TU1 functional. Dashed line, optical model (OM) analysis. Solid line, coupled channel (CC) calculation. The experimental data are from Ref. [57].

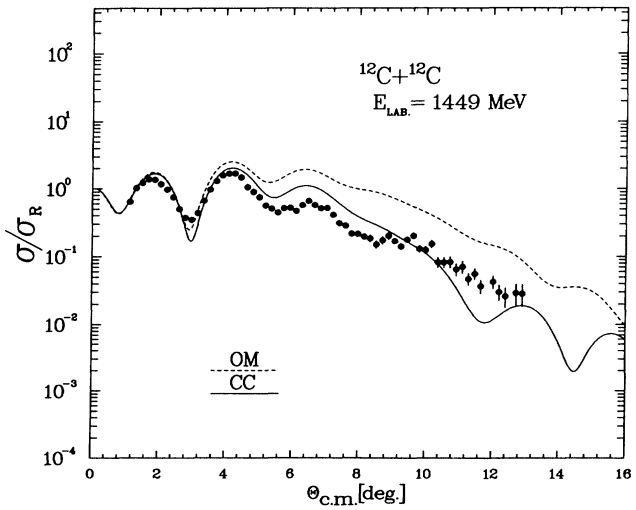

FIG. 8. Same as Fig. 7 for $E_{lab} = 1449$ MeV. The experimental data are from Ref. [58].

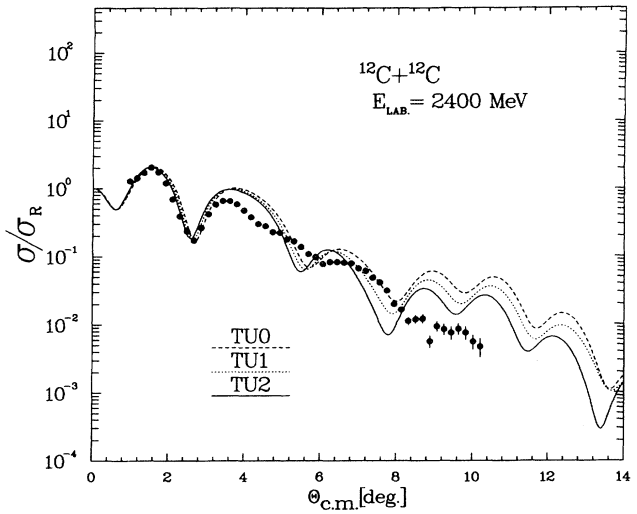

FIG. 9. Elastic scattering cross section for $^{12}C + ^{12}C$ at $E_{lab} = 2400$ MeV calculated in the CC analysis. Dashed line, using the TU0 functional; dotted line, TU1; and solid line, TU2. The experimental data are from Ref. [58].

data quite reasonably in the CC calculations. The role of the coupling to the lowest collective excitations in the colliding nuclei is substantial at the energies considered here. In other OM analysis using phenomenological optical potentials this effect is hidden by the adjustable parameters of the potentials and, consequently, little information about their explicit contribution to the cross section can be extracted. Comparing the OM and CC cross sections of the $^{12}C + ^{12}C$ reactions, we find that the effect of the 1p-1h contributions to the optical potential decreases with increasing energy. This shows the diminishing contribution of the nuclear surface excitations to the elastic scattering as the energy increases. The remaining discrepancy with the data, basically the

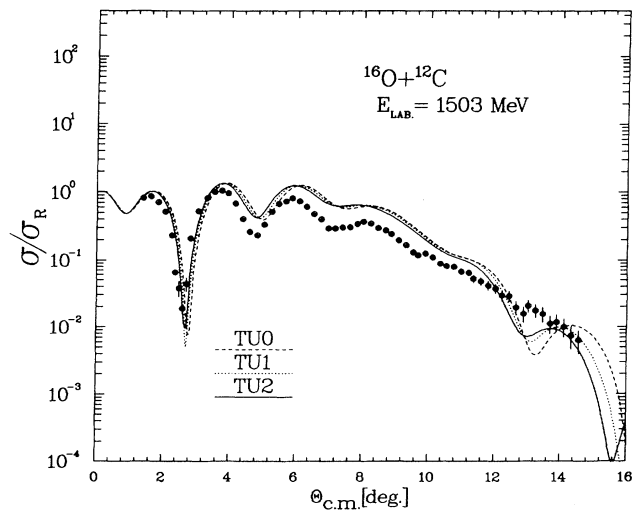

FIG. 10. Same as Fig. 9 for the system $^{16}O + ^{12}C$ at $E_{lab} = 1503$ MeV. The experimental data are from Ref. [59].

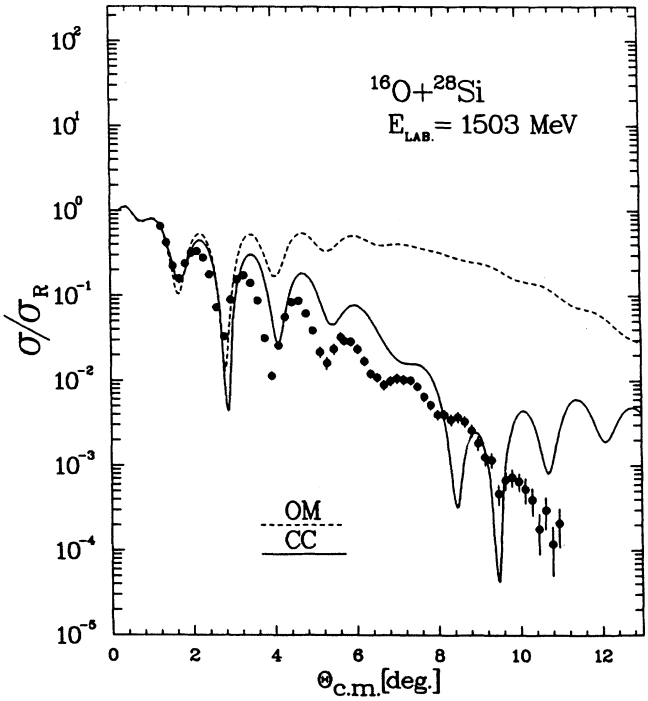

FIG. 11. Same as Fig. 7 for the system $^{16}O + ^{28}Si$ at $E_{lab} = 1503$ MeV. The experimental data are from Ref. [60].

lack of absorption, is expected to be due to other inelastic processes which are still not taken into account by the CC calculation, such as nucleon transfer between target and projectile, and especially alpha particle transfer [61] since these are $4n$ nuclei.

V. CONCLUSIONS

In this work we have studied the effects of the density-dependent Dirac spinor for the nucleons, as is determined microscopically in the DBHF approach, on various properties of the structure and scattering of finite nuclei. For this purpose, we have constructed a relativistic energy density functional that includes a volume part in the potential energy arising from a DBHF calculation of symmetric nuclear matter employing a realistic NN force [2, 3, 6]. This volume term is supplemented by the conventional correction terms accounting for the symmetry energy, the surface tension, and the Coulomb energy, and the relativistic kinetic energy density is corrected up to order $\hbar^2$ [35, 36]. The complete energy density functional contains three parameters which have been adjusted in such a way that a relativistic extended Thomas-Fermi (RETF) calculation of the binding energies of ^{40}Ca and ^{208}Pb and of the semiclassical fission barrier of ^{240}Pu (or the surface energy of semi-infinite nuclear matter) fits the experimental data. The parameter-free functional TU0, whose potential part is not affected by phenomenological parameters and only contains the Coulomb contribution in addition to the microscopic DBHF result, yields reasonable descriptions for ground-state properties of finite

nuclei and for HI optical potentials at intermediate incident energies, but it is not suitable for a calculation of fission barriers.

It turns out that the radii of nuclei calculated with the present approach agree better with the experimental value than those obtained in similar studies, using a potential energy derived from a nonrelativistic G matrix. This demonstrates that the Dirac effects improve the calculation of ground-state properties of finite nuclei also in our RETF approximation.

We want to stress, however, that this study of ground-state properties is not the main goal of our present investigation. For such studies direct microscopic calculations are possible [9] and other more sophisticated phenomenological relativistic models work well (see, e.g., [16, 17]).

The capabilities of our RETF functional are actually appraised in situations in which a microscopic relativistic calculation, or even a phenomenological one, cannot be easily made, such as nuclear fission of rotating nuclei and HI scattering. In these situations, the method constitutes a reliable tool. For the nuclear fission barriers, the present calculations are the first ones carried out with a relativistic model. We have shown that the model yields results comparable to the nonrelativistic ones with the conceptual advantage of being relativistic. For the HI elastic scattering cross section calculations, we have been able to improve the results the Tübingen group had previously obtained [34] due to achieving a better description of the nuclear densities.

The present calculations can be extended to finite temperatures, thus opening the possibility of exploring higher energy phenomena. Work along this line is now in progress.

ACKNOWLEDGMENTS

M.B. would like to thank the kind hospitality extended to him in Tübingen when this work was started. This work was supported in part by the GSI-Darmstadt and by the DGICYT (Spain) under Grant No. PB89-0332.

APPENDIX

In this appendix we give the explicit expression of the RETF kinetic energy density functional we use in Eq. (2.9). It has been obtained in a mean field semiclassical approach to the problem associated with a Dirac Hamiltonian which describes the single-particle motion of a set of fermions submitted to a scalar field and to the timelike component of a four-vector field. The reader is referred to [35, 36] for a detailed description of the method.

The RETF kinetic energy density of order $\hbar^2$ *for each kind of nucleon* is found to be

$$\tau = \tau_0 + \tau_2 , \tag{A1}$$

$$\tau_0 = \frac{1}{8\pi^2}\left[2k_F\varepsilon_F^3 - m^{*2}\left(5-4\frac{m}{m^*}\right)k_F\varepsilon_F + m^{*4}\left(3-4\frac{m}{m^*}\right)\ln\frac{k_F+\varepsilon_F}{m^*}\right] - m\frac{k_F^3}{3\pi^2} , \tag{A2}$$

$$\begin{aligned}\tau_2 = \frac{1}{72\varepsilon_F^2}\Bigg(&\left\{2k_F\left[1+2\left(1-\frac{m}{m^*}\right)\frac{m^{*2}}{\varepsilon_F^2}\right]\ln\frac{k_F+\varepsilon_F}{m^*} + \left(3-2\frac{m}{m^*}\right)\varepsilon_F - \left(1-\frac{m}{m^*}\right)\frac{m^{*2}}{\varepsilon_F}\right\}\frac{(\nabla\rho)^2}{\rho} \\ &+12\frac{m^*}{k_F}\left(1-\frac{m}{m^*}\right)\left[\frac{k_F}{\varepsilon_F} - \left(1-2\frac{m^{*2}}{\varepsilon_F^2}\right)\ln\frac{k_F+\varepsilon_F}{m^*}\right](\nabla\rho\cdot\nabla m^*) \\ &+\left\{\frac{9}{k_F}\left[3-4\left(1-\frac{m}{m^*}\right)\frac{m^{*2}}{\varepsilon_F^2}+\frac{m^{*2}}{k_F^2}\right]\ln\frac{k_F+\varepsilon_F}{m^*} - \frac{9}{\varepsilon_F}\left[1+3\left(1-\frac{m}{m^*}\right)+\frac{m^{*2}}{k_F^2}\right]\right\}\rho(\nabla m^*)^2\Bigg) ,\end{aligned} \tag{A3}$$

with $\varepsilon_F = (k_F^2 + m^{*2})^{1/2}$. The local Fermi momentum k_F is related to the particle density ρ through

$$k_F = \left(3\pi^2\rho\right)^{1/3} . \tag{A4}$$

In the nonrelativistic limit ($k_F \ll m$, $m^* \approx m$), one recovers from Eqs. (A1)–(A3) the well-known result [47]

$$\tau = \tau_0 + \tau_2 = \frac{3}{10m}(3\pi^2)^{2/3}\rho^{5/3} + \frac{1}{72m}\frac{(\nabla\rho)^2}{\rho} . \tag{A5}$$

[1] M. R. Anastasio, L. S. Celenza, W. S. Pong, and C. M. Shakin, Phys. Rep. **100**, 327 (1983); L. S. Celenza and C. M. Shakin, *Relativistic Nuclear Physics: Theories of Structure and Scattering* (World Scientific, Singapore, 1986).

[2] R. Brockmann and R. Machleidt, Phys. Lett. **149B**, 283 (1984).

[3] R. Machleidt and R. Brockmann, Phys. Lett. **160B**, 364 (1985).

[4] B. ter Haar and R. Malfliet, Phys. Rep. **149**, 207 (1987).

[5] R. Machleidt, Adv. Nucl. Phys. **19**, 189 (1989).

[6] R. Brockmann and R. Machleidt, Phys. Rev. C **42**, 1965 (1990).

[7] L. D. Miller and A. E. S. Green, Phys. Rev. C **5**, 241

(1972); L. D. Miller, *ibid.* **9**, 537 (1974).
[8] R. Brockmann, Phys. Rev. C **18**, 1510 (1978).
[9] H. Müther, R. Machleidt, and R. Brockmann, Phys. Lett. B **202**, 483 (1988); Phys. Rev. C **42**, 1981 (1990).
[10] K. W. Schmid, H. Müther, and R. Machleidt, Nucl. Phys. **A530**, 14 (1991).
[11] S. Marcos, M. López-Quelle, and Nguyen Van Giai, Phys. Lett. B **257**, 5 (1991).
[12] B. D. Serot and J. D. Walecka, Adv. Nucl. Phys. **16**, 1 (1986).
[13] P. -G. Reinhard, Rep. Prog. Phys. **52**, 439 (1989).
[14] C. J. Horowitz and B. D. Serot, Nucl. Phys. **A368**, 503 (1981).
[15] A. Bouyssy, S. Marcos, and Pham Van Thieu, Nucl. Phys. **A422**, 541 (1984).
[16] P. -G. Reinhard, M. Rufa, J. Maruhn, W. Greiner, and J. Friedrich, Z. Phys. A **323**, 13 (1986).
[17] Y. K. Gambhir, P. Ring, and A. Thimet, Ann. Phys. (N.Y.) **198**, 132 (1990).
[18] A. Bouyssy, J. -F. Mathiot, Nguyen Van Giai, and S. Marcos, Phys. Rev. C **36**, 380 (1987).
[19] P. G. Blunden and M. J. Iqbal, Phys. Lett. B **196**, 295 (1987).
[20] T. H. R. Skyrme, Philos. Mag. **1**, 1043 (1956).
[21] D. Vautherin and D. M. Brink, Phys. Rev. C **5**, 626 (1972).
[22] D. Gogny, in *Proceedings of the International Conference on Nuclear Self-consistent Fields*, Trieste, 1975, edited by G. Ripka and M. Porneuf (North-Holland, Amsterdam, 1975).
[23] S. Marcos, R. Niembro, M. López-Quelle, Nguyen Van Giai, and R. Malfliet, Phys. Rev. C **39**, 1134 (1989).
[24] H. Elsenhans, H. Müther, and R. Machleidt, Nucl. Phys. **A515**, 715 (1990).
[25] S. Gmuca, J. Phys. G **17**, 1115 (1991).
[26] R. Brockmann and H. Toki, Phys. Rev. Lett. **68**, 3408 (1992).
[27] S. -J. Lee, J. Fink, A. B. Balantekin, M. R. Strayer, A. S. Umar, P. -G. Reinhard, J. A. Maruhn, and W. Greiner, Phys. Rev. Lett. **57**, 2916 (1986); **59**, 1171 (1987).
[28] W. Pannert, P. Ring, and J. Boguta, Phys. Rev. Lett. **59**, 2420 (1987).
[29] C. E. Price and G. E. Walker, Phys. Rev. C **36**, 354 (1987); R. J. Furnstahl, C. E. Price, and G. E. Walker, *ibid.* **36**, 2590 (1987).
[30] Z. Y. Zhu, H. J. Mang, and P. Ring, Phys. Lett. B **254**, 325 (1991).
[31] J. -K. Zhang and D. S. Onley, Nucl. Phys. **A526**, 245 (1991).
[32] K. -H. Müller, Nucl. Phys. **A372**, 459 (1981).
[33] R. Y. Cusson, P. -G. Reinhard, J. J. Molitoris, H. Stöcker, M. R. Strayer, and W. Greiner, Phys. Rev. Lett. **55**, 2786 (1985).
[34] N. Ohtsuka, M. Shabshiry, R. Linden, H. Müther, and Amand Faessler, Nucl. Phys. **A490**, 715 (1988).
[35] M. Centelles, X. Viñas, M. Barranco, and P. Schuck, Nucl. Phys. **A519**, 73c (1990).
[36] M. Centelles, X. Viñas, M. Barranco, and P. Schuck, Ann. Phys. (N.Y.) (to be published).
[37] F. Garcias, M. Barranco, Amand Faessler, and N. Ohtsuka, Z. Phys. A **336**, 31 (1990).
[38] M. Centelles, X. Viñas, M. Barranco, N. Ohtsuka, Amand Faessler, Dao Tien Khoa, and H. Müther, J. Phys. G **17**, L193 (1991).
[39] E. Engel and R. M. Dreizler, Phys. Rev. A **35**, 3607 (1987).
[40] M. K. Weigel, S. Haddad, and F. Weber, J. Phys. G **17**, 619 (1991).
[41] C. Speicher, R. M. Dreizler, and E. Engel, Ann. Phys. (N.Y.) **213**, 312 (1992).
[42] M. Centelles, X. Viñas, M. Barranco, S. Marcos, and R. J. Lombard, Nucl. Phys. **A537**, 486 (1992).
[43] H. Müther, M. Prakash, and T. L. Ainsworth, Phys. Lett. B **199**, 469 (1987).
[44] G. Q. Li, R. Machleidt, and R. Brockmann, Phys. Rev. C **45**, 2782 (1992).
[45] M. Centelles, M. Pi, X. Viñas, F. Garcias, and M. Barranco, Nucl. Phys. **A510**, 397 (1990).
[46] M. Brack, Jens Damgaard, A. S. Jensen, H. C. Pauli, V. M. Strutinsky, and C. Y. Wong, Rev. Mod. Phys. **44**, 320 (1972).
[47] M. Brack, C. Guet, and H. -B. Håkansson, Phys. Rep. **123**, 275 (1985).
[48] J. Treiner and H. Krivine, Ann. Phys. (N.Y.) **170**, 406 (1986).
[49] A. J. Sierk, Phys. Rev. C **33**, 2039 (1986).
[50] W. D. Myers, *Droplet Model of Atomic Nuclei* (IFI/Plenum, New York, 1977).
[51] S. Cohen, F. Plasil, and W. J. Swiatecki, Ann. Phys. (N.Y.) **82**, 557 (1974).
[52] W. D. Myers and W. J. Swiatecki, Ann. Phys. (N.Y.) **211**, 292 (1991).
[53] T. Izumoto, S. Krewald, and Amand Faessler, Nucl. Phys. **A341**, 319 (1980); **A357**, 471 (1981).
[54] N. Ohtsuka, R. Linden, Amand Faessler, and F. B. Malik, Nucl. Phys. **A465**, 550 (1987).
[55] M. H. Macfarlane and S. C. Pieper, Argonne National Laboratory Report ANL-76-11, 1978.
[56] S. B. Khadkikar, L. Rikus, Amand Faessler, and R. Sartor, Nucl. Phys. **A369**, 495 (1981).
[57] M. Buenerd, A. Lounis, J. Chauvin, D. Lebrun, P. Martin, G. Duhamel, J. C. Gondrand, and P. de Saintignon, Nucl. Phys. **A424**, 313 (1984).
[58] J. Y. Hostachy, M. Buenerd, J. Chauvin, D. Lebrun, Ph. Martin, J. C. Lugol, L. Papineau, P. Roussel, N. Alamanos, J. Arvieux, and C. Cerruti, Nucl. Phys. **A490**, 441 (1988).
[59] P. Roussel, N. Alamanos, F. Auger, J. Barrette, B. Berthier, B. Fernandez, L. Papineau, H. Doubre, and W. Mittig, Phys. Rev. Lett. **54**, 1779 (1985).
[60] P. Roussel, J. Barrette, F. Auger, B. Berthier, B. Fernandez, J. Gastebois, A. Gillibert, L. Papineau, W. Mittig, D. Disdier, B. Lott, V. Rauch, F. Scheibling, C. Stephan, and L. Tassan-Got, Phys. Lett. B **185**, 29 (1987).
[61] J. Diaz, J. L. Ferrero, J. A. Ruiz, B. Bilwes, and R. Bilwes, Nucl. Phys. **A494**, 311 (1989).